High Enthalpy Flow Characterization
Using Tunable Diode Laser Absorption Spectroscopy

Ciro Salvi[*][†]*, Lars Steffens*[*]*, Oliver Hohn*[*]*, Ali Gülhan*[*]*, and Filippo Maggi*[**]

[*]*German Aerospace Center (DLR)*
51147 Köln, Germany

[**]*Politecnico di Milano*
20156 Milano, Italy

[†]Corresponding author: ciro.salvi@dlr.de

Abstract

This research aims at analysing thermo-chemical properties of the hypersonic high-enthalpy flow in the L2K wind tunnel, situated in Köln at the German Aerospace Center (DLR). In the L2K wind tunnel, Martian atmosphere can be created, and the facility can simulate heat load conditions encountered during atmospheric entry of Martian missions. The focus of this project is the analysis of the non-intrusive experimental technique "Tunable Diode Laser Absorption Spectroscopy" (TDLAS), based on line of sight absorption spectroscopy, and applied to hypersonic flow. A simplified Martian atmosphere (97% CO_2 and 3% N_2) was used. A new interpretation for CO-TDLAS experimental technique applied to hypersonic wind tunnel flow analysis was developed. Numerical simulations with the DLR-TAU non-equilibrium flow solver were used as support of this analysis, and match between simulations and experiments was observed. Flow speed and absorption line's width were measured, and the knowledge of L2K's flow structure was extended.

1. Introduction

Experimental characterization of Thermal Protection Systems (TPS) materials and flight instrumentation at Martian entry conditions require partially significant changes to the nominal operation mode of existing long duration high-enthalpy facilities. Therefore, for the characterization of combined sensors of the ESA ExoMars 2016 instrumentation package COMARS+ and test of the TPS materials, the arc-heated facility L2K (figure 1) was upgraded in terms of operation and measurement techniques. This data was also used for the validation of numerical tools. This study aims at analysing thermo-chemical properties of the hypersonic high-enthalpy flow field of the L2K by using further diagnostics.

The *Supersonic and Hypersonic Technologies Department* in Köln owns the LBK facility, composed by two high-enthalpy parallel wind tunnels – the L2K and the L3K – capable of simulating atmospheric entry of spacecrafts. In the L2K wind tunnel, different flow compositions can be used, to simulate the atmospheres of our Earth, Mars, and Titan. LBK wind tunnels are certified by ESA as European key testing facilities for TPS. The survivability of spacecrafts in atmospheric entry is provided by TPS, whose behaviour must be accurately studied in characteristic testing facilities able to reproduce high heat flux phases of atmospheric entry for long times, and arc-heated high-enthalpy wind tunnels such as the LBK complex best suit these requirements, at the expense of aerodynamic properties characterization [1, 2]: the low density environment causes Reynolds number to be too low compared to atmospheric entry. In such conditions it is important to consider a reacting non-equilibrium flow [3]. It is of main interest to characterize wind tunnels flows [4] for multiple purposes, such as to to get more information about the flow field, to obtain meaningful results from test campaigns, to know which limits and which strengths these facilities have, and to gain knowledge of critical aspects of hypersonics, since flow characterization provides interpretation tools to experimental results and flow phenomena. For chemically reacting flows, chemical composition analysis is needed, which requires challenging experimental techniques, based mainly on spectroscopy. In addition, characterization of wind tunnels' flows allows validation of numerical models, and deepens knowledge about hypersonic flows phenomena [1]. L2K flow was simulated in Takahashi's work [5] and Lantelme's thesis [6], where non-equilibrium Martian atmosphere was considered.

This work extends the knowledge of L2K's flow when Martian atmosphere is simulated, exploiting absorption spectroscopy [7]. Analysed flow conditions were defined by DLR in the post-flight analysis of ESA ExoMars 2016 mission

(a) L2K test section and diffusor
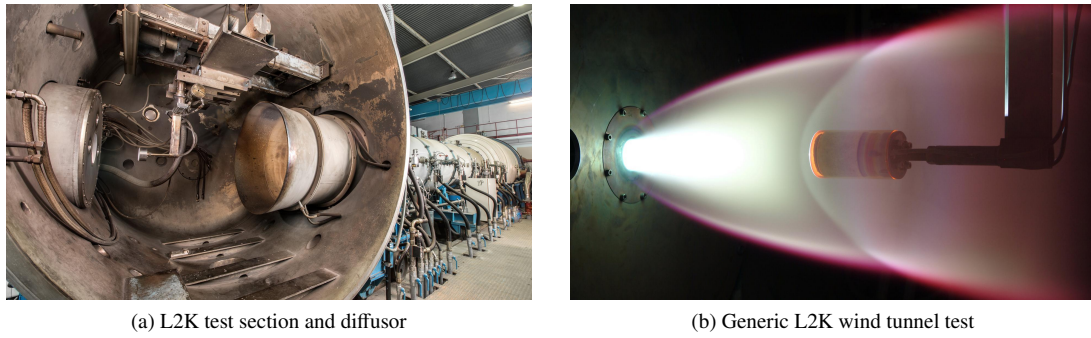

(b) Generic L2K wind tunnel test

Figure 1: The L2K high-enthalpy wind tunnel

[8], and are reported in table 1. Specific flow conditions need to be analysed both energetically (such work was carried in [6]) and chemically. Numerical simulations with DLR-TAU flow solver were performed as support of this analysis. As reported in [5], Pitot pressure, heat flux, and mass-averaged enthalpy of arc-heated flows have been experimentally obtained in the past; non-intrusive techniques such as Laser Induced Fluorescence (LIF) and Tunable Diode Laser Absorption Spectroscopy (TDLAS) [9] have been used to determine distributions of rotational and translational temperature, flow velocity and number density. In [10] and [11] Argon flows were studied in the L2K wind tunnel, while in [12] TDLAS technique was applied to a hypersonic impulse facility; in [13] TDLAS was used in an arc jet facility, and a mismatch between expected and evaluated temperature was highlighted.

The most important outcome of this project is the definition of a new method of interpretation of L2K - TDLAS data, that could explain the mismatch between expected temperature and TDLAS temperature found in [13]. A deep understanding of TDLAS applied to non-homogeneous hypersonic flow analysis is reported; the definition of a line-shape model for non-intrusive Line of Sight (LOS) measurement techniques is presented, along with the physical interpretation of experimental results.

In the following sections, the experimental setup and mathematical modelling of TDLAS data will be presented; then, numerical and experimental results will be reported; in the end, conclusions and outlook will be given.

2. Modelling and Setup

As reported in [5], L2K reservoir is energized by a 1.4 MW Huels-type arc heater which grants the flow a high specific enthalpy thanks to the electrical discharge; flow conditions can be varied with different degrees of freedom, such as mass flow rate, reservoir pressure[1], nozzle exit diameter, sample position, and chamber background pressure, which grant a wide range of operating conditions of the testing facility[2]; heat flux varies also on flow axis, thanks to nozzle's geometry, that causes flow post-expansion. A broad selection of intrusive and non-intrusive measurement techniques can be used (for instance, thermocouples, thermocameras, pyrometers, Pitot probes, TDLAS, Laser Induced Fluorescence or LIF, Fourier Trasform IinfraRed spectroscopy or FTIR). L2K nozzle geometry to be used is reported in figure 2, and flow conditions to be analysed are reported in table 1, as in [6]. The prescribed measurement positions are on flow axis, at a distance from the nozzle exit of $x = \{100, 200, 300\}$ mm. The experimental setup is described in detail in section 2.2.

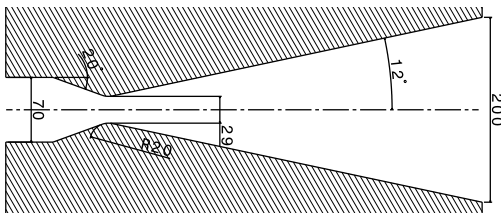Figure 2: L2K nozzle geometry, *200 mm* exit diameter configuration

Table 1: Flow conditions.

Parameter		FCI	FCII
Total mass flow rate	$\dot{m}$ [g/s]	41.2	
Mass flow rate CO_2 (97%)	$\dot{m}_{CO_2}$ [g/s]	40	
Mass flow rate N_2 (3%)	$\dot{m}_{N_2}$ [g/s]	1.2	
Reservoir pressure	p_{res} [hPa]	790	930
Predicted specific enthalpy*	h [MJ/kg]	5.6	9.2
Predicted reservoir temperature*	T_{res} [K]	2815	3283
*Estimated with quasi-1D flow solver NATA in [6]			

[1]Given a maximum installed power, maximum heat flux and maximum stagnation pressure are competing parameters: to obtain high stagnation pressure, high mass flow rates must be selected, reducing the specific enthalpy of the flow, and so its temperature and heat flux on the sample.

[2]Large test section, Mach number reaching up to 8, tunable mass flow rate (5 to 125 g/s), specific enthalpy of 10 MJ/kg at mass flow rate of 50 g/s, heat flux of 4 MW/m^2, stagnation pressures of 250 hPa [5] and maximum test duration of 2 h, make L2K very versatile.

2.1 Spectroscopic Model

Absorption phenomena can be modelled with the spectral-directional Beer-Lambert law [14, 15], considering an absorption path s:

$$T_\lambda = \frac{I}{I_0} = e^{-\int_0^L \alpha_\lambda(s)ds} = e^{-\tau_\lambda} \tag{1}$$

The subscripts λ indicate that the quantity is spectral, i.e. depending on wavelength λ (or, dually, on wavenumber $\nu = 1/\lambda$); T_λ is the spectral transmittance, I and I_0 are the transmitted and incident radiations respectively, α_λ is the spectral attenuation (or absorption) coefficient, τ_λ is the spectral optical depth, and L is the length of the absorption path. Isolated absorption lines (i.e. spectral optical depth) can be modelled with the Voigt profile, as a trade-off between complexity and accuracy. The Voigt profile is in fact characterized by only four parameters, according to [16]:

1. *Peak position* ν_0, namely the wavenumber coinciding to the maximum absorption. It is determined by the ideally absorbed photon's energy in vacuum; it is shifted if other molecules are in proximity of the absorbing molecule (pressure-induced shift), and if the absorbing gas is moving (Doppler effect).
2. *Intensity* τ^*, namely the integral of the absorption line. It depends on temperature, line constants and energy level.
3. *Doppler broadening* γ_D, namely the energy dispersion caused by molecules' chaotic motion.
4. *Collisional broadening* γ_C, namely the energy dispersion caused by finite lifetime of excited states.

Voigt profile's parameters are related to flow characteristics via the following relations, taken from [17]. Pressure-induced peak shift was neglected. Light source quality was hypothesized ideal, since its broadening is $\gamma < 10^{-2} \ m^{-1}$, as stated in [9]; on the other hand, collisional and Doppler broadening were considered in modelling absorption lines. Voigt profile is the convolution of Lorentz profile $L(\nu, \gamma_C)$ and Gauss profile $G(\nu, \gamma_D)$, as reported in equation 2. An absorption line simulator related to flow characteristics was implemented in Matlab, and validated against `hapi.py`, HITRAN Application Programming Interface [18, 19]. The validation process highlighted a relative deviation of 0.5%[3].

$$V(\nu, \gamma_D, \gamma_C) = \int_{-\infty}^{+\infty} G(\nu', \gamma_D) L\left((\nu - \nu'), \gamma_C\right) d\nu' \tag{2}$$

The following relations are reported from [17]. Knowing the unitary-integral Voigt absorption profile centered on the absorption wavenumber ν_0, namely $V_\nu(\nu_0, \gamma_D, \gamma_C)$, the molecular absorption coefficient can be expressed as:

$$\alpha'_\nu(\nu_0, \gamma_D, \gamma_C) = S_{ij} V_\nu(\nu_0, \gamma_D, \gamma_C) \tag{3}$$

where S_{ij} is the tabulated transition intensity. The measured absorption line (namely the dimensionless optical depth τ_ν) is the integration along the absorption path of the molecular absorption lines, scaled by the local number density n_i, that can be evaluated as $n_i = p/(kT)$, where k is the Boltzmann constant:

$$\tau_\nu(\nu_0, T, p) = \int_0^L \alpha'_\nu(\nu_0, T, p) n_i ds \tag{4}$$

If constant properties can be assumed along s, equation 4 can be simplified:

$$\tau_\nu(\nu_0, T, p) = \alpha'_\nu n_i L \tag{5}$$

The intensity of an absorption line τ^* can be defined as the area under the absorption line itself. The integral of the Voigt-shaped absorption line τ^*, assuming constant properties along s, is equal to the line's transition intensity multiplied by the column density $n_i L$, since the integral of a Voigt profile on wavenumber is unitary:

$$\tau^* = \int_0^\infty \tau_\nu(\nu_0, T, p) d\nu = \int_0^\infty \alpha'_\nu(\nu_0, T, p) n_i L d\nu = \int_0^\infty S_{ij} V_\nu(\nu_0, T, p) n_i L d\nu = n_i L S_{ij} \tag{6}$$

Collisional and Doppler broadening contribute to the overall Half Width Half Maximum (HWHM) of the absorption line. *Doppler broadening* γ_D can be modelled as fully dependent on temperature:

$$\gamma_D(T) = \frac{\nu_0}{c} \sqrt{\frac{2kT \ln 2}{M_m}} \tag{7}$$

---

[3]Line profile simulation in Matlab was performed with Voigt mathematical model, and molecular intensity and the integral of the simulated profile coincide; on the other hand, `hapi.py` uses the PCQSDHC routine (Partially-Correlated Quadratic-Speed-Dependent Hard-Collision) for line simulation, which leads to a mismatch between profile's integral and molecular intensity of 0.5%. The source of the mismatch is unclear. Voigt mathematical model was used for simplicity.

HIGH ENTHALPY FLOW CHARACTERIZATION USING TDLAS

Collisional broadening γ_C, on the other hand, depends on pressure and temperature; in particular, each species "i" in the mixture contributes to the overall collisional broadening via its molar fraction χ_i and its broadening coefficient $\gamma_i(p, T)_{ref}$ measured in reference conditions ($p_{ref} = 1$ *atm* and $T_{ref} = 296$ *K*):

$$\gamma_C(p, T) = \left(\frac{T_{ref}}{T}\right)^n p \sum_i \left[\gamma_i(p, T)_{ref}\, \chi_i\right] \tag{8}$$

In the wind tunnel conditions, the absorption profile is temperature-dominated, since pressure value is relatively low; thus, collisional broadening can be neglected, and flow pressure cannot be retrieved from absorption data.
Once the absorption line of a mixture is measured, it is necessary to fit the Voigt model to experimental data with non-linear optimization, thus retrieving its four parameters *position, intensity, Doppler broadening, collisional broadening*. Knowing ν_0, M_m, S_{ij}, $\gamma_i(p, T)_{ref}$ and n from HITRAN, knowing the absorption path length L and the observation angle ε_0 (refer to figure 4a) from setup geometry in CAD, it is possible to retrieve line parameters from nonlinear fitting. If properties of the absorbing gas are constant, temperature can be evaluated from Doppler broadening γ_D, as:

$$T = \frac{M_m}{2k \ln(2)} \left(\frac{c\gamma_D}{\nu_0}\right)^2 \tag{9}$$

Note that, in the L2K arc-heated wind tunnel, constant properties cannot be assumed and T cannot be evaluated with equation 9. From absorption line intensity τ^*, and knowing S_{ij}, number density can be estimated:

$$n_i = \frac{\tau^*}{S_{ij}L} \tag{10}$$

If the observed absorbing species are moving with respect to the observer, a Doppler shift $\Delta\nu$ of the central absorption wavenumber will be observed, which is related to relative flow speed Δv: $\Delta\nu = \nu_0 \Delta v / c$, where c is the speed of light.

2.2 Experimental Setup: TDLAS

Tunable Diode Laser Absorption Spectroscopy (TDLAS or DLAS) technique consists in using a narrow band diode laser whose peak can be shifted in wavelength, up to few *nm*; this feature can be used to scan narrow spectra, around a central wavelength where an absorption line is expected. TDLAS can be used for flow analysis: it is a non-intrusive technique that permits to measure flow speed, temperature and observed species' concentration; however, it suffers from LOS-integrated effects, such as Doppler dispersion and chamber effects, later discussed.
A scheme of the TDLAS setup is reported in figure 3. The laser beam is splitted in two coherent branches, one used for signal calibration, and one for flow analysis. The latter enters the chamber and crosses flow axis with a defined observation angle ε_0, as in figure 4a. The oscilloscope is used in DC coupling, storing 20 *ksamples* with 10^{-7} *s* sampling time, and a resolution of 10^{-6} *V*; it is triggered on modulation signal.
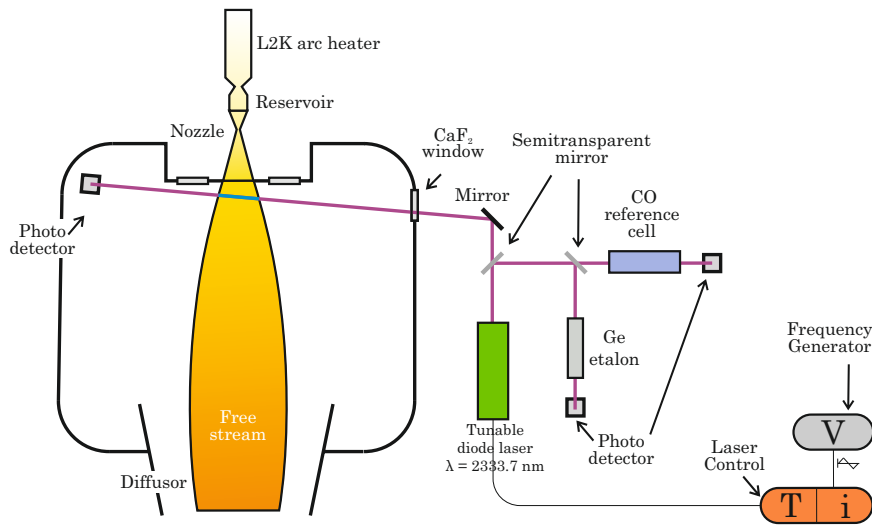

Figure 3: Conceptual scheme for TDLAS measurements

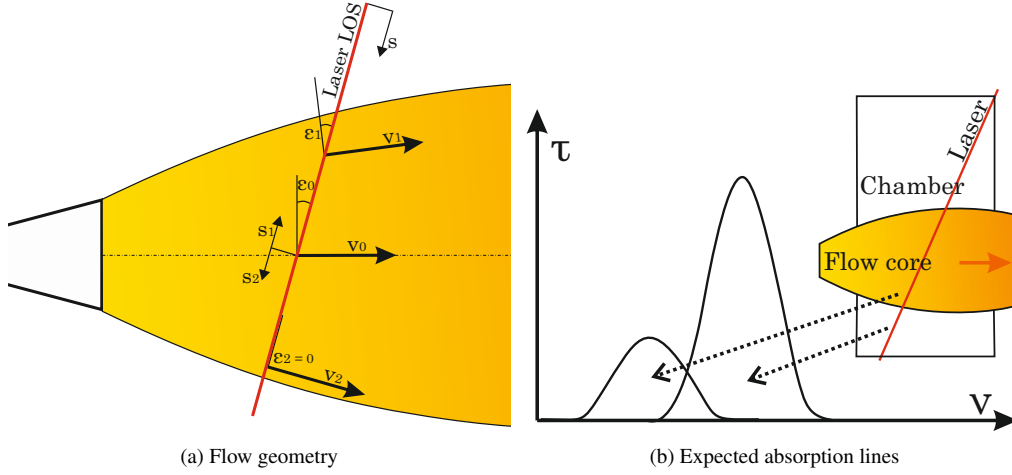(a) Flow geometry

(b) Expected absorption lines

Figure 4: Flow model and absorption features model

The expected LOS-projected absorption spectrum obtained would be composed by two main features, as sketched in figure 4b: the prominent absorption line on the right is caused by CO accumulated in the chamber, and the smaller one on the left is caused by CO in the flow. Simulations highlighted that the assumption of constant properties along the LOS (such as mentioned in [9]) must be dropped, thus flow temperature cannot be straightforwardly estimated with equation 9.

However, from flow's absorption line, gas speed can be estimated: knowing peak position of the resting gas of a reference cell and the tilt angle ε_0 between laser's LOS and flow velocity's perpendicular, flow velocity is related to peak shift $\Delta\nu$ via Doppler effect:

$$v = \frac{\Delta v}{\sin\varepsilon} = \frac{c\Delta\nu}{\nu_0 \sin\varepsilon} \tag{11}$$

The two photo-detectors will measure a decrease of light intensity in correspondence of the absorption line, and from their output, the absorption line can be reconstructed as in [12].

The tunable diode laser permits to scan on a sufficiently broad range of wavelengths to identify absorption lines; the possible wavelength span should be at least 4-to-5 times higher than the expected line broadening. The used diode laser is *DL 100 DFB* from TOPTICA Photonics [20], centered on $\lambda = 2333.7$ *nm*. Laser's wavelength λ can be varied with two parameters, namely temperature T and current intensity i; in its design point, *DL 100 DFB* emits at $\lambda = 2333.7$ *nm*, with $T = 32°$ and $i = 136$ *mA*. From technical specifications, T, i, and λ have lower and upper limits:

$$T \in (15, 40) \ °C \qquad\qquad i \in (57, 180) \ mA \qquad\qquad \lambda \in (2329.1, 2335.1) \ nm$$

From HITRAN database [17, 21–24] the central absorption wavelengths of all the expected species in the flow can be found in the laser's λ range; analysed species are[4] CO_2, CO, O_2, N_2, O, NO, N, C_2, C, CN, NCO; only CO has a detectable intensity, thus the analysis can be made only on Carbon Monoxide with this laser. Data from HITRAN are reported in table 2, where S_{ij} $[(cm^{-1})/(molecule \cdot cm^{-2})]$ is the spectral line intensity, A_{ij} $[s^{-1}]$ is the Einstein-A coefficient of a transition, E'' $[cm^{-1}]$ is the lower state energy of the transition, i and j are the global upper and lower quanta, and $\gamma_{CO_2,CO}$ $[m^{-1}/atm]$ are the CO_2-broadened and self-broadened HWHM at $T_{ref} = 296$ K and $p_{ref} = 1$ *atm*.

Table 2: Absorption line data from HITRAN database

Line	Isotope	λ [nm]	ν [cm^{-1}]	S_{ij} [$\cdot10^{-21}$]	A_{ij}	E''	$i \rightarrow j$	γ_{CO_2}	n_{CO_2}	γ_{CO}
R7	$^{12}C^{16}O$	2331.9	4288.3	3.47	0.52	107.6	$8 \rightarrow 7$	7.67	0.65	5.4

The modulator signal was chosen as a triangular, which grants linear relation between current and time; the modulation signal shape choice allows simplification in data processing, bringing linear relations between λ and t. However, it was observed that for high modulation frequencies a linear relation between modulation input and laser output *cannot* be assumed, as damping is introduced. Signal regions affected by non-linearities are discarded in signal processing.

---

[4]These species were evaluated with NATA code in [6].

Modulation signal cannot be used as a baseline in data post processing, due to time shift and damping. Modulation frequency was set to 1 kHz, as a trade-off between data quality and laser output linearity.

From the raw data reported in figure 5a one can extract the sweeps reported in figure 5b that will be processed. To extract the sweeps, non-linear regions must be removed. If one sweep is incomplete, it is discarded and not analysed. Then, a conversion from time to λ domain was performed thanks to calibration with Etalon. Etalon signal's local maxima are tracked and assigned an incremental ID_i function of time t_i, as in figure 5b.
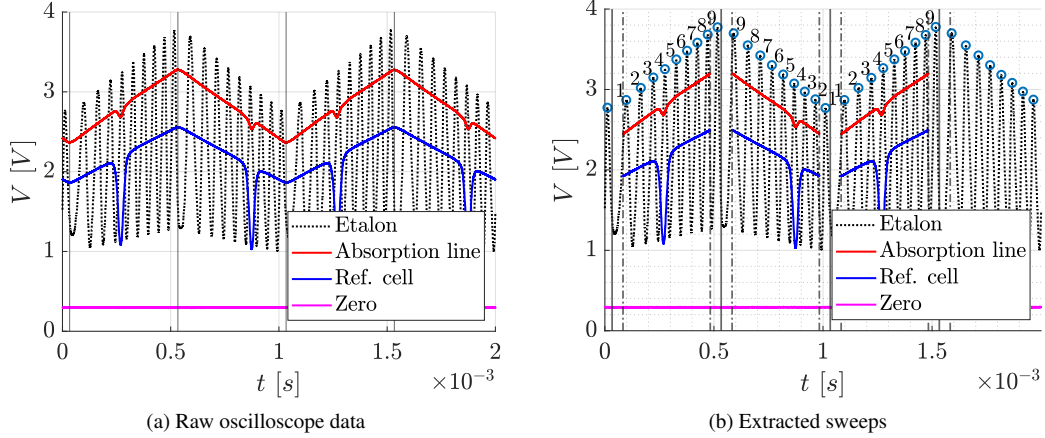

(a) Raw oscilloscope data

(b) Extracted sweeps

Figure 5: DLAS data extraction

Conversion is possible if the Free Spectral Range (FSR or $\delta\lambda_i$, namely the separation between two adjacent maxima) of the Etalon is known. Etalon's FSR depends on interferometer's physical parameters and beam's wavelength [25]:

$$\delta\lambda_i = \frac{\lambda_{0_i}^2}{2n_g l \cos\theta + \lambda_{0_i}} \simeq \frac{\lambda_{0_i}^2}{2n_g l \cos\theta} \tag{13}$$

where n_g is the group refractive index of the interferometer mirrors, l is their separation length, and θ is the inclination between interferometer mirror and incident radiation.

For the chosen Germanium Etalon, $n_g = 4 \pm 0.2$ (5%)[5], $l = (50 \pm 0.15 \ (0.3\%))$ mm[6], and $\theta = (0 \pm 1.2)°$[7]; λ_0 can be assumed constant as its variation is in the order of Angstroms, and the relative error introduced is $10^{-3}\%$. For the observed absorption line centered on $\lambda_0 = 2331.9$ nm, the expected FSR is $\delta\lambda_i = 0.0136$ nm.

The polynomial regression's statistical error of the time conversion (reported to 1σ) is 0.3%.

Once the signal has been reported to differential wavenumber domain, transmission coefficient T_ν (or $T_{\Delta\nu}$) and optical depth τ_ν can be evaluated as in equations 1 and 14; the sensor's zero must be known to determine signal's offset, thus the real I value; zero signal is reported in figure 5a, and its average value was used to determine transmission.

$$T_\nu = \frac{I(\nu)}{I_0(\nu)} \qquad\qquad \tau_\nu = -\ln T_\nu \tag{14}$$

$I_0(t)$, namely the incident radiation, can be retrieved with in the following way: assuming that only the sweep's central part is subject to absorption (this is valid for high modulation amplitude), the I_0 signal can be constructed by using the two extremal non-absorbing regions of the sweep itself: polynomial fittings on these two regions can be performed; the central region can be constructed as a cubic polynomial matching the two extremal parts, with continuous derivative, as shown in figure 6a.

The signal is affected by high-frequency mechanical noise, even if stabilizers and dampers were used, due to wind tunnel's vibrations, caused probably by the pumping system. Transmission and absorption values are related by logarithmic relation and are reported in figure 6b. Reported values are *differential-spectral*, i.e. depending on $\Delta\nu$ (or $\Delta\lambda$). They can be reported to absolute wavelength, using the reference cell.

On the global optical depth, fitting operation can be performed to find the two absorption lines corresponding to chamber and flow regions (according to the model presented in figure 4b). In figure 7, the processed spectra of FCII with nozzle exit diameter of 200 mm are reported; in the reported spectra one can observe that the two main regions

---

[5]The uncertainty was evaluated considering average Germanium n_g values in literature, since no datasheet is provided.

[6]From manufacturing tolerance.

[7]Assuming 1 mm rotational shift in Etalon placement, the relative uncertainty on $\cos\theta$ is $2 \cdot 10^{-2}$ %.

(a) I_0 signal construction

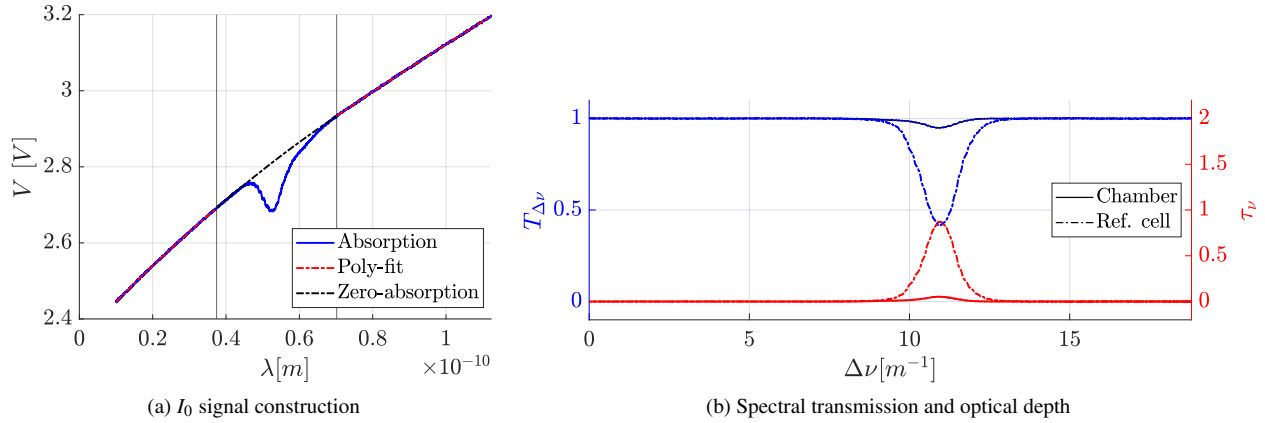(b) Spectral transmission and optical depth

Figure 6: TDLAS data process

related to the chamber's *CO* and the flow's *CO* are not well-distinguished. The solution of a *least-square* problem is required; Matlab's built-in function `lsqnonlin.m` was used, with *trust-region-reflective* algorithm, which showed more robustness than the *Levenberg-Marquardt*. To monitor the fitting process, R-squared value R^2 and the normalised residual are evaluated to discuss quality of the fitting line. In figure 7 one exemplar absorption pattern is reported; fitting residual and R^2 are reported.

(a) Optical depth, sweep 1
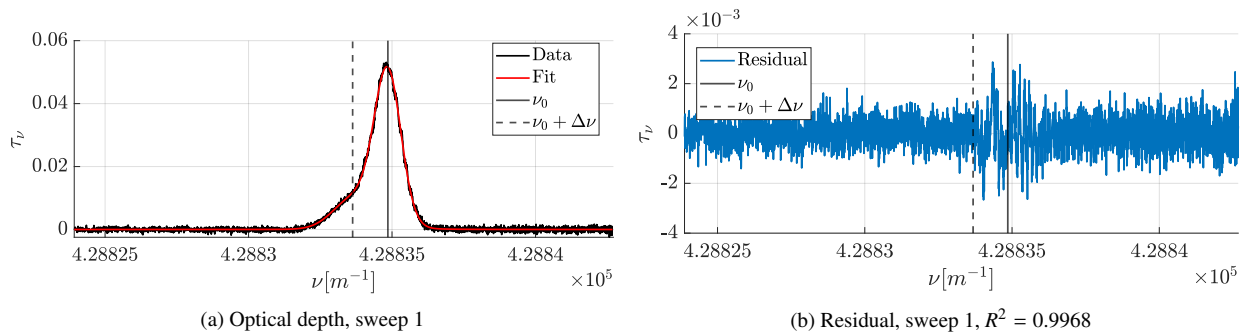
(b) Residual, sweep 1, $R^2 = 0.9968$

Figure 7: TDLAS data fit

Collisional and Doppler broadening γ_D and γ_C associated to the Voigt profiles can be found after fitting. After the first experimental analysis where constant properties were assumed in the observed regions, a consistent mismatch between the expected and the evaluated flow temperature was observed. To explain this mismatch, a new interpretation of the absorption line is necessary, since the free stream expands in the test section; as a result:

- The flow velocity component tangent to the laser's LOS varies along the LOS itself, causing the central absorption wavelength to vary along the absorption path. This causes a dispersion of the local contributions to the overall absorption line, causing additional broadening (**LOS-parallel velocity dispersion**).
- If the LOS is not perpendicular to flow axis, the **absorption feature is asymmetric** between the two sides of laser's LOS, namely *laser's side* (between laser and flow axis) and *sensor's side* (between flow axis and sensor).

According to Beer-Lambert law (equation 1), the flow's absorption profile results as the integral of the infinitesimal absorption profiles along the LOS, depending on local temperature, pressure, velocity, and number density, and the hypothesis of constant properties along the LOS must be dropped.
On the other hand, flow surroundings can be modelled with one single Voigt absorption profile, since chamber's gas motion was assumed negligible, and diffusion times are hypothesized short enough to consider constant properties. One can eventually measure chamber pressure and temperature from the absorption spectra.

2.2.1 The "BLOB" Profile

According to the model presented in figure 4a, the observation angle ε between the LOS and the flow velocity's perpendicular varies along the absorption path s. As a consequence, the Voigt absorption bell corresponding to an in-

finitesimal absorption path will be shifted with respect to a fixed ν_0 by a certain value $\Delta\nu$, depending on the observation angle through the Doppler effect: $\Delta\nu = \nu_0 v \sin\varepsilon/c$. On flow axis, $\varepsilon = \varepsilon_0$ is known and depends on setup geometry. On flow boundaries, $\varepsilon = \varepsilon_b$ can be estimated with optical measurements. For highly post-expanding flows, ε may become null and negative. For this reason a LOS-parallel velocity ($v_\parallel = v \sin\varepsilon$) dispersion is present.

The global absorption profile τ can be evaluated as the integral of the infinitesimal absorption profiles given by infinitesimal absorption path ds. Eventually, for axialsymmetric geometries, two absorption regions can be defined, with coordinates s_1 and s_2 from flow axis, as in figure 4a.

The Voigt profile was assumed for each infinitesimal absorption path: $\alpha'_\nu(\nu_0, \gamma_D, \gamma_C, S) = S_{ij} V(\nu_0, \gamma_D, \gamma_C)$. The four parameters characterizing the local absorption profile can be retrieved knowing local T, p, χ, and v, which in turn depend on s. The resulting absorption profile was named as the "BLOB" profile B_ν, which stands for "Broadening by LOS-Overlayed Bells"; the BLOB dispersion accounts for all causes of dispersion (namely *collisions broadening*, *Doppler broadening* and *LOS-parallel velocity dispersion*) and can be described as:

$$B_\nu = \int_L \alpha_\nu\left(\nu_0(s), \gamma_D(s), \gamma_C(s), S_{ij}(s)\right) ds = \int_L \alpha_\nu(s)\, ds = \int_0^{L_1} \alpha_\nu(s) ds_1 + \int_0^{L_2} \alpha_\nu(s) ds_2 \qquad (15)$$

Results from CFD simulations were used to evaluate properties on the laser's LOS, which geometrically intersects flow axis and has a fixed access window, to simulate the BLOB profile with equation 5, in the validated Matlab routine. Three different measurement positions were considered (thus three different LOS), in compliance with test campaign: the laser must intersect flow axis at *100, 200* and *300 mm* from the nozzle exit position.

The LOS is discretized in a total of 200 points (100 for the laser side and 100 for the sensor's side), whose coordinates are used in an interpolation routine that aims at extracting numerical simulations' data on the LOS. The discretization of the LOS is performed in equal segments, and properties are considered constant on each segment.

2.3 Numerical Setup

For numerical simulations, DLR-TAU solver was used, and high temperature effects and chemical reactions were considered, since the expected reservoir temperature is above 3000 *K* and since chemical composition of the flow needs to be retrieved, both for BLOB simulation and for validation of numerical simulations. Due to the 2-components Martian atmosphere used in the prescribed flow conditions (reported in table 1), a 11-species/103-reactions chemical model was chosen, which accounts for the chemical compounds CO_2, CO, O_2, O, NO, N_2, N, C, $C2$, CN, NCO, that can react as described in [26–28]. Non-equilibrium solver was used. Computations are performed in steady flow field. Due to the high stiffness of the problem caused by different time scales of the different hypersonic physical phenomena, a 2D axialsymmetric geometry with structured mesh was chosen to reduce the computational effort. 91122 nodes are present in the computational domain, as a trade-off between accuracy and speed. According to the sensitivity study reported in [6], such number of nodes is more than sufficient to have mesh-independent results.

3. Results

In this section, experimental and numerical results are reported. Finally, the BLOB profile simulation is compared against experimental data, and experimental results are discussed.

3.1 Numerical Results

Numerical simulations of the present work were validated by comparison with results obtained in [6]; a detailed analysis of flow properties is reported in the mentioned work.

Final results for FCII are reported in figure 8. The two flow conditions differ in quantitative results, due to the different reservoir pressure condition. In particular, higher reservoir pressure leads to higher flow enthalpy, thus velocity and Mach number, whereas flow temperature and pressure are lower for higher reservoir pressure conditions. This counter-intuitive phenomenon is due to the different level of dissociation of Carbon Dioxide between the two conditions, which is lower for lower reservoir pressure conditions, as confirmed by experimental results reported in figure 11.

Thermochemical flow properties retrieved with numerical simulations were interpolated on the laser's LOS (figure 9a), to simulate the global expected absorption line, in agreement with the BLOB integral model mentioned in section 2.2.1. From figure 9b one may notice the high in-homogeneity and non-symmetry of the component of flow velocity tangent to the laser's LOS, namely: $v_\parallel = v \sin\varepsilon$. This parameter determines the absorption line's peak position. Such in-homogeneity suggests that a single-bell model for the flow's absorption line is inappropriate yet inaccurate: flow's

(a) Axial velocity v_z

(b) Radial velocity v_z

(c) CO mass fraction

(d) Temperature

Figure 8: DLR-TAU flow solver solution, FCII

(a) LOS interpolation tool

(b) $v_{\parallel}$ value, for all measurement positions
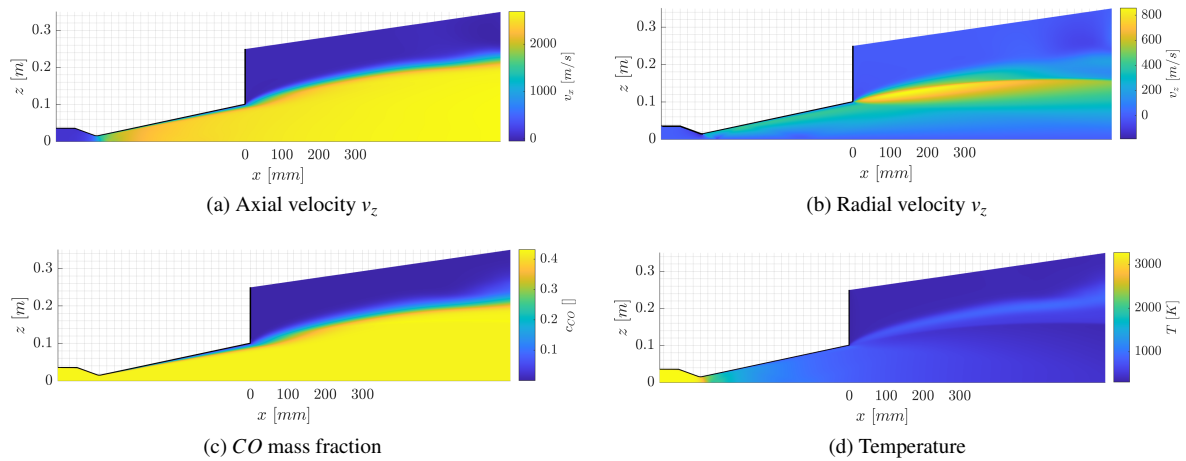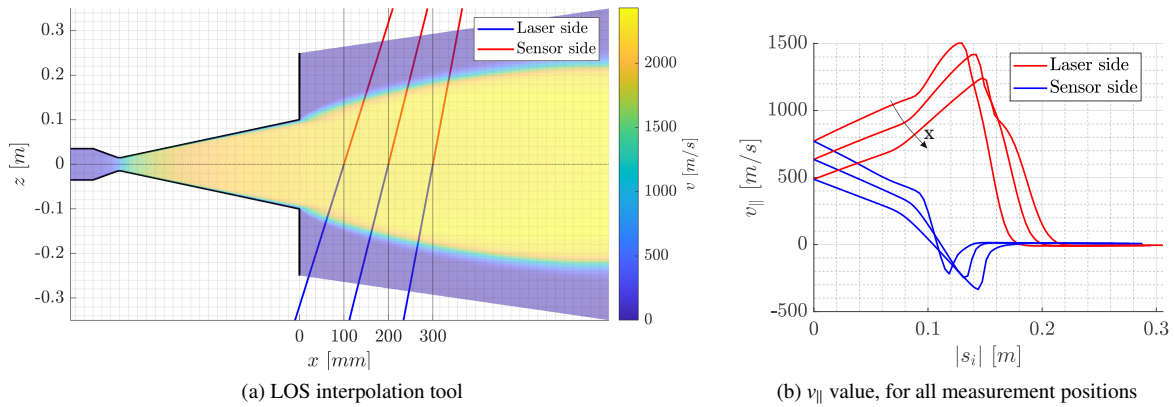
Figure 9: Interpolation of flow properties for BLOB simulation

post-expansion determines a Doppler-dispersion of the absorption line's partial contributions, as reported in figure 10a. This effect is due to flow geometry that presents a high radial component of velocity, as reported in figure 8b.

The overlay of the partial contributions in figure 10a − scaled accordingly to the length of the discretization step of the LOS − builds up the numerical BLOB profile, which is reported in figure 10b. The result depends on the discretization step length, and it converges to the reported profile with the used discretization. The dashed line in 10b represents the one-bell expected absorption profile if constant properties along the LOS (tangent velocity, temperature, molar fraction, pressure) are considered. The two models − integral BLOB and one-bell − clearly show different features; in particular, BLOB profile intensity is lower, and its FWHM is higher. These effects are due to the in-homogeneity of CO molar fraction along the absorption path and to the LOS-parallel velocity dispersion of the local contributions, respectively. The comparison between experimental data and the simulated absorption line with BLOB theory is reported in figure 10b: simulations quite well match experimental results for this condition, but no chamber line is resolved by the simulation, since the current numerical setups do not resolve chamber's CO. This is because the whole chamber including the diffusor was not simulated, thus the recirculation process later described is not resolved; however, this should not affect the flow's absorption line consistently, since its hypersonic nature. For this reason, a slightly off-nominal experimental condition (chamber pressure: $p_c = 0.59$ $mbar$) was used for comparison, in figure 10b, which is later discussed in section 3.2.1.

BLOB properties behaviour with respect to flow properties variation was analysed by exploring of a 4-dimensional grid of proportionality parameters, one related to each property of numerical results (*axial velocity*, *radial velocity*, *CO molar fraction* and *temperature*). By scaling these properties, artificially-built flow conditions can be used to study how the BLOB profile can vary. Due to the non-physicality of this scaling process, and the intrinsic uncertainty in numerical results, the performed analysis is supposed to give only qualitative results, and to get familiarity with the LOS-parallel velocity dispersion (or BLOB effect) of expanding flows. Main conclusions are here reported:

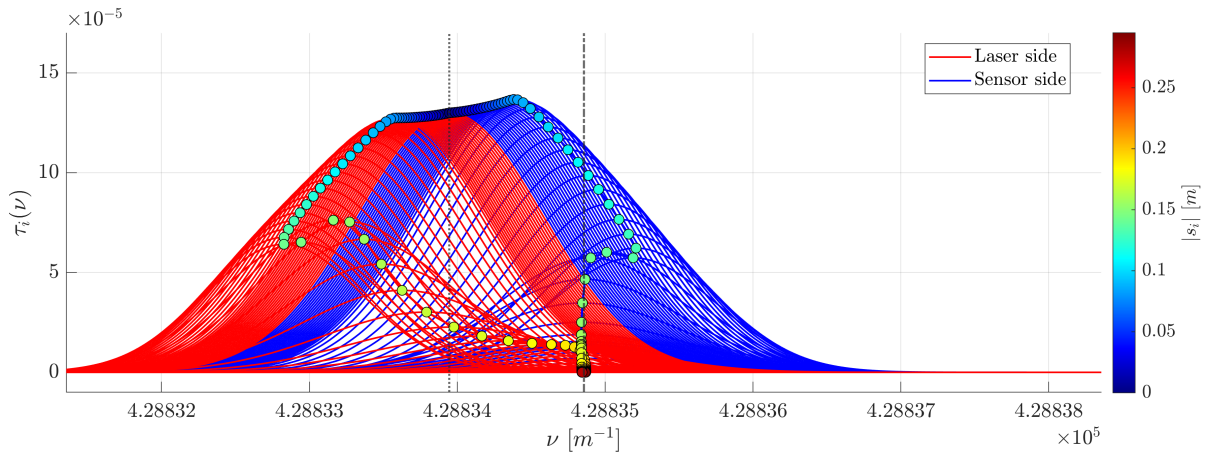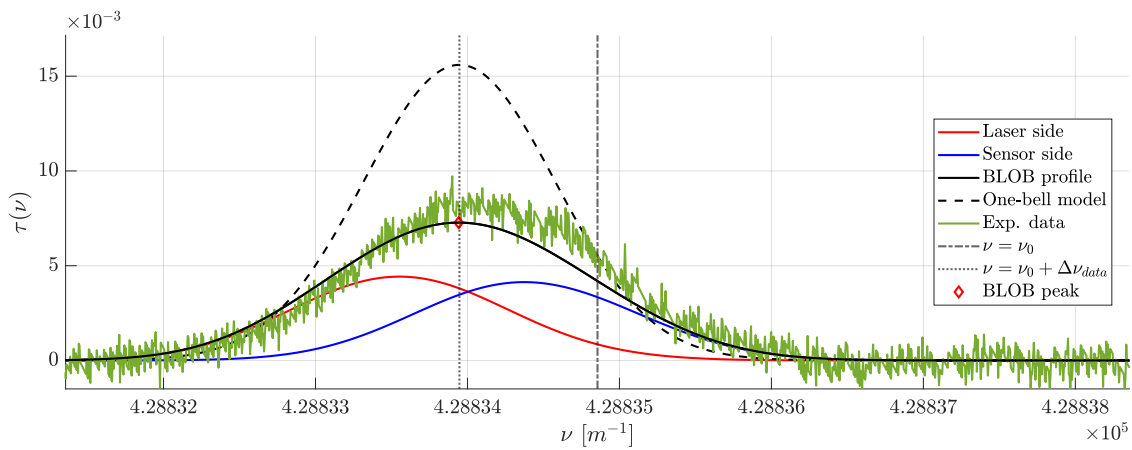- BLOB effect does not bring high uncertainty on the axial velocity estimation, since BLOB peak is for every

(a) BLOB partial spectra, for measurement position $x = 200\ mm$

(b) BLOB profile compared with experimental data, for measurement position $x = 200\ mm$

Figure 10: BLOB profile simulation and experimental data

    condition close to the one-bell model peak, and highly depends on axial velocity only; negligible dependencies were noted between peak position and other flow parameters.

- BLOB's Full Widths at y-Maximum[8] (*FWyM*), as well as its second order momentum, on the other hand, depend both on temperature and radial velocity; no dependencies with axial velocity is noted.
- Left-side and Right-side Slopes at y-Maximum[8] (*LSyM, RSyM*) depend both on temperature and molar fraction.

3.2 Experimental Results

A validation process highlighted that pressure is not well estimated in the wind tunnel's conditions, due to its low value: line's broadening is highly temperature-dominated, leading to high uncertainty on pressure estimation, as confirmed by monitoring confidence intervals of the fitting algorithm's output.

Absorption spectra of FCI and FCII with 200 *mm* exit diameter nozzle, on different measurement positions x are reported in figure 11, where one may observe that the chamber's and flow's absorption lines are not well distinguishable for some conditions. In addition, the absorption profiles change with measurement position and flow condition. In particular, the higher the measurement position, the lower the observation angle ε_0, the lower the separation between flow bell and chamber bell. Moreover, FCII is characterized by higher absorption values: higher reservoir pressure and temperature bring higher dissociation, meaning higher CO molar fraction inside flow and chamber.

Despite dependencies between flow properties and flow absorption line were noted, analysis of experimental results presents some intrinsic difficulties which make the estimation of flow properties uncertain. For the analysed flow conditions, the chamber's absorption bell hides the flow's absorption bell, which is not easily recognisable by the

---

[8] $y = \{0.25, 0.5, 0.75\}$. For $y = 0.5$, *FWyM = FWHM*.

fitting algorithm. It was noted that flow bell is more recognisable for higher observation angles and conditions where chamber absorption line is less prominent, which are discussed in section 3.2.1.

(a) Measurement position $x = 100mm$

(b) Measurement position $x = 200mm$

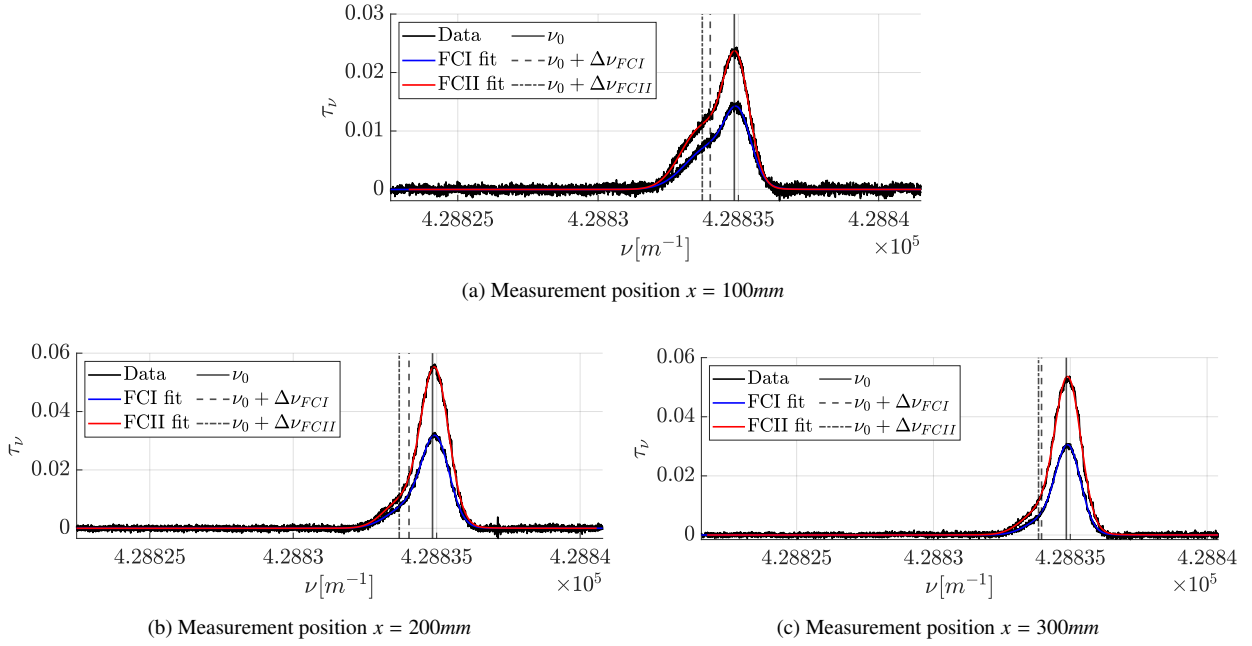(c) Measurement position $x = 300mm$

Figure 11: Experimental results, only one sweep is reported

3.2.1 Post-expansion effect

L2K flow picture is reported in figure 12 for same reservoir conditions as FCII; one may observe its post-expansion due to nozzle's non-adaptation and conical shape. The post-expansion is determined by the pressure difference between flow and chamber's background pressure p_c: with the same conditions of reservoir pressure and chamber pressure, smaller nozzle's exit diameter d_e determines lower expansion in the nozzle, which causes a more aggressive post-expansion in comparison with larger exit diameter nozzle; with the same conditions of reservoir pressure and nozzle diameter, the post-expansion is milder for higher background pressure.
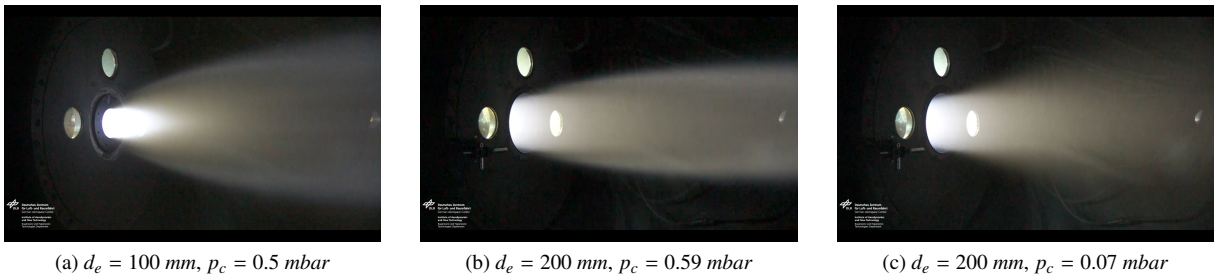

(a) $d_e = 100\ mm$, $p_c = 0.5\ mbar$

(b) $d_e = 200\ mm$, $p_c = 0.59\ mbar$

(c) $d_e = 200\ mm$, $p_c = 0.07\ mbar$

Figure 12: Flow geometry

Post-expansion affects the absorption profile, as reported in figure 13: varying the cold-flow valve aperture in L2K − a valve that regulates the outer air inflow to have a degree of freedom on background pressure and regulate flow properties −, from the minimum value of 0% to the maximum value of 35%, the chamber's absorption line shows a rapid intensity decrease between apertures of 25% and 30%; a possible explanation to this phenomenon is: at low background pressure, the external flow layers don't enter perfectly the test chamber's diffusor, causing an internal recirculation of CO; at high background pressure, the flow fits perfectly the diffusor, causing the chamber's absorption line to disappear. Note that the red absorption feature was obtained artificially by subtracting the fitted chamber's Voigt-shaped absorption line to the experimental data.

Experimental results are reported in figure 14 and in table 3; total uncertainty u_{tot} is evaluated combining statistic uncertainty $u_S = \sigma / \sqrt{N}$ and systematic uncertainty u_B with RSS.
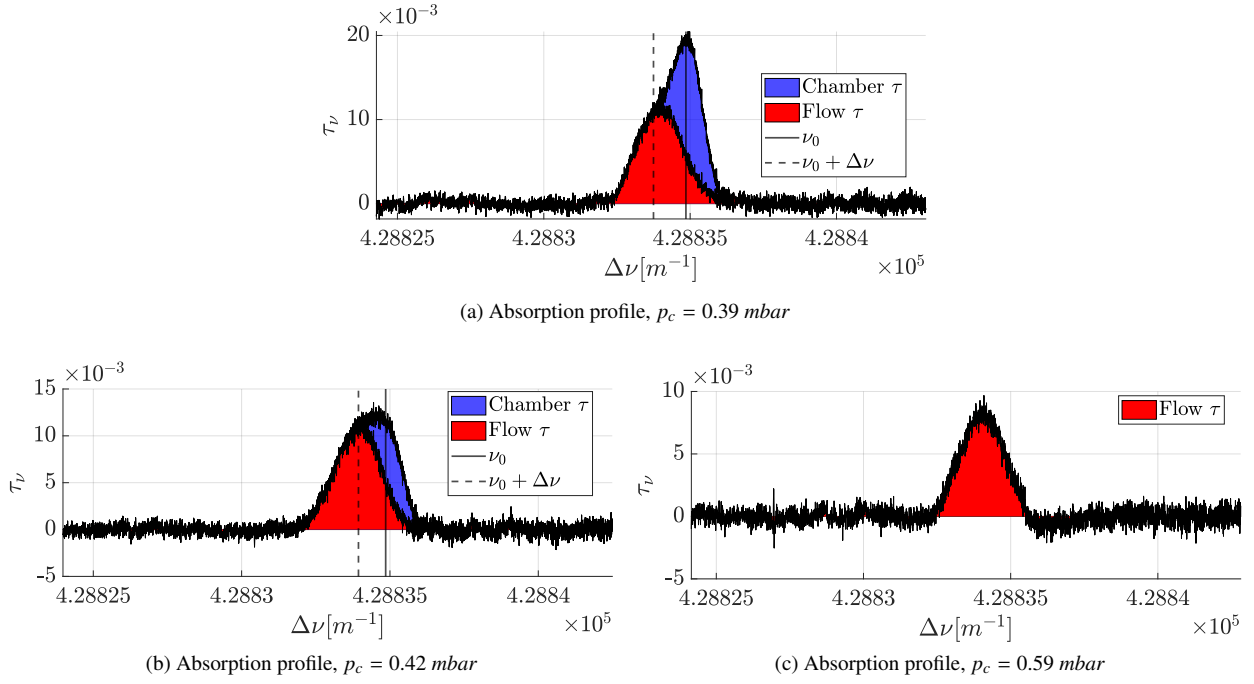
HIGH ENTHALPY FLOW CHARACTERIZATION USING TDLAS

(a) Absorption profile, $p_c = 0.39$ *mbar*

(b) Absorption profile, $p_c = 0.42$ *mbar*

(c) Absorption profile, $p_c = 0.59$ *mbar*

Figure 13: FCII, background pressure and absorption profiles

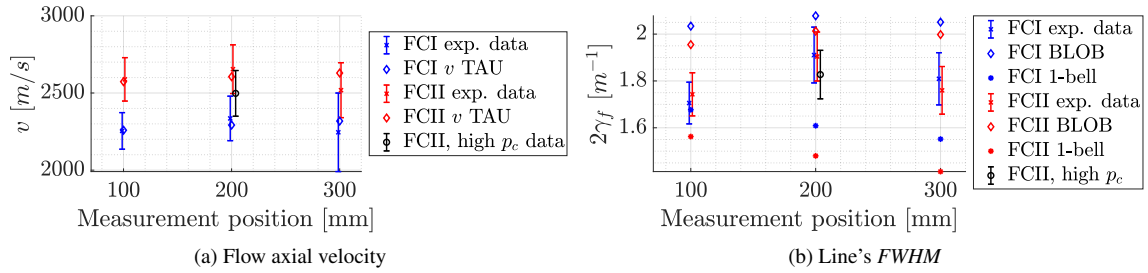(a) Flow axial velocity

(b) Line's *FWHM*

Figure 14: Experimental results

In figure 14, results are graphically reported for both flow conditions, for all measurement positions, in terms of flow axial velocity, and flow line's *FWHM*, or $2\gamma_f$; *FWHM* cannot be related to temperature uniquely. Results are reported as error bars in figure 14, in blue for FCI and red for FCII.

In addition, expected values from numerical simulations and models are reported as discrete points:

a. Expected flow axial speed in figure 14a comes from numerical results.

b. Two types of expected *FWHM* are reported in figure 14b, according to two different models, namely the one-bell model (the asterisks), dependent uniquely on temperature and pressure, and the simulations accounting for BLOB effects compliant with TAU results (the diamonds), reported in section 3.1.

Note that results *for same measurement position* are slightly shifted on *x* for visualization purposes only.

In figures 14a and 14b, the black error bar is referred to a test condition different from the nominal one, performed on measurement position $x = 200$ *mm*. Same reservoir conditions as FCII were used, but a different value of cold flow was selected to obtain the highest background pressure possible, namely $p_c = 0.59$ *mbar* (in nominal conditions, $p_c = 0.35$ *mbar*). The high background pressure, as reported in figure 13c, allows clear resolution of the flow's absorption line, permitting lower uncertainty on *FWHM* value. Note that this result cannot be compared quantitatively to other results, since the different background pressures result in different flow conditions, which won't match the available numerical simulations, that would require different boundary conditions setup.

From figure 14, the following observations have emerged:

• Axial speed is well estimated for both flow conditions, for measurement positions $x = \{100, 200\}$ *mm*. High background pressure condition brings lower flow speed.

- Flow line's *FWHM* is not well estimated neither by the one-bell model (except for FCI, at $x = 100\ mm$) nor by the BLOB simulations, since experimental values lay in between the two models' predictions. Experimental results' trend shows better agreement with BLOB simulations, with respect to one-bell model, which is monotonically decreasing. Experimental results, cross-checked with high background pressure results, show that line properties interpretation (BLOB effect) is correct, since *FWHM* does not follow the temperature trend, being dependent on other quantities. However, a too high BLOB dispersion was predicted, due to a possible mismatch between numerical simulations and flow properties (for instance, the simulated post-expansion may be too high).
- Flow line's *FWHM* of FCI and FCII is larger than flow line's *FWHM* of high background pressure condition: as expected, higher background pressures causes milder post-expansion, thus lower BLOB dispersion.
- Measurement position $x = 300\ mm$ suffers high uncertainty for all quantities, since observation angle is smaller, and the two lines are not well separated; on the contrary, $x = 100\ mm$ measurement position shows the highest precision.

Results and total uncertainties are reported in table 3 for each measurement position $x = \{100, 200, 300\}\ mm$.

Table 3: Experimental results, nominal conditions

| | | **FCI, $d_e = 200\ mm$** | | |
		$x = 100\ mm$	$x = 200\ mm$	$x = 300\ mm$
v	$[m/s]$	$2254 \pm 118\ (5.3\%)$	$2335 \pm 144\ (6.2\%)$	$2245 \pm 254\ (11.3\%)$
$2\gamma_f$	$[m^{-1}]$	$1.71 \pm 0.10\ (5.2\%)$	$1.91 \pm 0.12\ (6.2\%)$	$1.81 \pm 0.11\ (6.1\%)$
		FCII, $d_e = 200\ mm$		
		$x = 100\ mm$	$x = 200\ mm$	$x = 300\ mm$
v	$[m/s]$	$2588 \pm 141\ (5.4\%)$	$2654 \pm 158\ (5.9\%)$	$2518 \pm 188\ (7.1\%)$
$2\gamma_f$	$[m^{-1}]$	$1.74 \pm 0.09\ (5.3\%)$	$1.90 \pm 0.10\ (5.5\%)$	$1.76 \pm 0.10\ (5.8\%)$

4. Conclusions

This experimental activity focused on analysing defined flow conditions in the hypersonic wind tunnel L2K with *CO*-TDLAS. This analysis answered why TDLAS analysis in L2K flow cannot determine flow temperature with standard equations from absorption theory, assuming constant properties on the laser's line of sight.

A new method of interpretation of TDLAS data was developed, bringing to a new understanding of IR spectroscopic data in the arc-heated wind tunnel. The observed absorption line is to be considered as the overlay of the LOS-dependent contributions on the optical depth. In other words, the profile in figure 10 allows to observe that the broadening effect of the overall absorption line is mainly due to the flow's post-expansion: the parallel velocity in-homogeneity along the LOS (well observable in figure 10a) causes local contributions to be dispersed on the spectra. The BLOB (Broadening by LOS-Overlayed Bells) model developed for absorption feature interpretation is described in section 2.2.1. Its simulations are shown in figure 10. Flow post-expansion causes in first place a high radial velocity at the exit of the nozzle, which in turn drives the $v_{\parallel}$ dispersion. As observed in the reported results, this effect must be considered when analysing post-expanding or non-adapted flows.

In addition, the chamber's absorption line is prominent in the analysed flow conditions, causing additional difficulty in identifying the correct flow's absorption profile. Chamber line's prominence reduces if the background pressure is incremented, since when the flow is adapted to the diffusor, the recirculation of *CO* inside the chamber is reduced. These phenomena highlight the difficulty of analysing L2K flow, pointing out the challenges of studying hypersonic flows. However, it might be possible to analyse flow properties in some conditions, characterized by a non-prominent chamber's absorption line (namely, with high background pressure or small absorption path inside the chamber), and by high separation of the two absorption lines (namely, in high-velocity conditions or with a high observation angle ε_0).

The simulated and the experimental lines have similar profiles, as shown in figure 10b: simulations are well-estimating *CO* concentration in the flow. On the other side, the two profiles show different broadening: simulated flow geometry is not perfectly matching reality, being slightly more post-expanded; this causes a larger LOS-parallel velocity dispersion which could explain this mismatch. Note that such considerations can be done only if the flow's absorption line is well distinguishable from the chamber's absorption line (i.e. high background pressures are chosen). Moreover, figure 10b shows the good match on absorption line location, meaning that the numerical setup is well-estimating velocity. However, figure 14b shows that numerical results overestimate BLOB broadening, thus simulations should be adjusted to match experimental data.

4.1 Further Improvements and Outlook

- In principle it could be possible to extract empirical relations with BLOB simulations for different flow conditions: many numerical simulations should be performed, and adapted to the available measurements of the test chamber, matching for instance flow geometry, which could require much computational effort.
- From figure 10a it was observed that four flow regions can be identified: a *central core* with constant CO molar fraction and linear $v_\parallel$, an *outer core* with higher $v_\parallel$ variation (due to post-expansion) and decreasing CO, an *inner shear layer* with decreasing $v_\parallel$ and CO molar fraction and high temperature, and an *outer shear layer* whose properties tend to chamber properties. A 4-bells model should be developed and tuned to the fitting algorithm, to assess the possibility of retrieving flow properties, eventually in different regions.
- A study on the area of the isolated flow absorption line should be performed, since it is a parameter directly related to CO concentration (equation 10). This study, in comparison with BLOB simulations coming from TAU results, could be a complete validation source for TAU solver, regarding the accuracy on the degree of dissociation of CO_2. This procedure shall be performed in conditions where the flow is observable with no chamber-related disturbances. However, note that since the technique is affected by LOS effect, the validation cannot be performed on local values of CO concentration, but on its integral value (which is related to the average value of CO concentration).
- The laser's LOS can be translated in parallel to scan the flow, and with Abel transformation one may obtain space-resolved results, since the flow can be assumed axialsymmetric.

5. Acknowledgments

References

[1] J. M. A. Longo, K. Hannemann, and V. Hannemann. The challenge of modelling high speed flows. In *EUROSIM*, Ljubljana, 9–13 Sept., 2007.

[2] B. Esser, A. Gülhan, A. del Vecchio, S. Löhle, Nicolas Sauvage, Olivier Chazot, and Cem O. Asma. Comparative heat flux measurements on standard models in plasma facilities. *AIAA Paper No. 2005-3324*.

[3] J. D. Anderson Jr. *Hypersonic and High-Temperature gas Dynamics, 3rd Edition*. AIAA Education, Reston, Virginia, 2019.

[4] B. Esser and A. Gülhan. Flow field characterization of DLR's arc-heated facilities L2K and L3K. In *3rd European Symposium on Aerothermodynamics for Space Vehicles*, Noordwijk, 24-26 Nov., 1998.

[5] T. Takahashi, B. Esser, L.Steffens, and A. Gülhan. Plasma flow modeling for huels-type arc heater with turbulent diffusion. *Physics of Plasmas*, 24:123509, 2017.

[6] M. T. Lantelme. Energetic Characterization of Martian Atmospheric Flow in the Arc-Heated Wind Tunnel L2K Using Experimental and Numerical Methods. Master's thesis, Karlsruhe Institute of Technology, DLR, 2020.

[7] U. Koch and A. Gülhan. Technical report on DLAS and emission spectroscopy. Report D34.1, DLR, Cologne, 2016.

[8] ESA. ExoMars 2016 Schiaparelli Descent Sequence. `https://exploration.esa.int/web/mars/-/57465-exomars-2016-schiaparelli-descent-sequence`. Accessed: 22-07-2022.

[9] J. Riehmer. Charakterisierung des strömungsfeldes in der lichtbogenbeheizten versuchsanlage des DLR in Köln mit laserinduzierter fluoreszenz und laserdiodenspektroskopie [Characterisation of the flow field in the L2K using laser induced fluorescence and diode laser spectroscopy]. Bachelor's thesis, Institut fur Raumfahrtsysteme, Universitat Stuttgart, 2007.

[10] U. Koch, B. Esser, L.Steffens, and A. Gülhan. Flow Characterization and MHD Test in High Enthalpy Argon Flows. In *8th European Symposium on Aerothermodynamics for Space Vehicles*, Lisbon, 2-6 Mar., 2015.

[11] U. Koch, B. Esser, L.Steffens, and A. Gülhan. Characterization of weakly ionized argon flows for radio blackout mitigation experiments. *Progress in Flight Physics*, 9:335–348, 2017.

[12] J. M. Meyers, S. Paris, and D. G. Fletcher. Characterization of CO_2 flow in a hypersonic impulse facility using DLAS. *Experiments in Fluids*, 57:25, 2016.

[13] R. Vallon, J. Soutadé, J. Vérant, J. Meyers, S. Paris, and A. Mohamed. A Compact Tunable Diode Laser Absorption Spectrometer to Monitor CO_2 at $2.7\mu m$ Wavelength in Hypersonic Flows. *Sensors*, 10:6081–6091, 2010.

[14] T. G. Mayerhöfer, S. Pahlow, and J. Popp. The Bouguer-Beer-Lambert Law: Shining Light on the Obscure. *ChemPhysChem*, 21:2029–2046, 2020.

[15] IUPAC. *Compendium of Chemical Therminology, 2nd edition (The "Gold Book")*. Blackwell Science, Oxford, 1997.

[16] HITRAN. Definitions and units: Line-by-line parameters. `https://hitran.org/docs/definitions-and-units/`. Accessed: 22-07-2022.

[17] HITRAN. The HITRAN DATABASE. `https://hitran.org/`. Accessed: 22-07-2022.

[18] R.V. Kochanov, I.E. Gordon, L.S. Rothman, P. Wcisło, C. Hill, and J.S. Wilzewski. HITRAN Application programming interface (HAPI): a comprehensive approach to working with spectroscopic data. *Journal of Quantitative Spectroscopy & Radiative Transfer*, 177:15–30, 2016.

[19] Roman V. Kochanov. HITRAN Application Programming Interface (HAPI). User Guide Ver. 4.3, 2019.

[20] Anon. DL 100 DFB Production & Quality Control Data Sheet. TOPTICA Photonics, Order n. VB.07.0583, 2007.

[21] I. E. Gordon, L. S. Rothman, R. J. Hargreaves, R. Hashemi, E. V. Karlovets, F. M. Skinner, E. K. Conway, C. Hill, R. V. Kochanov, Y. Tan, P. Wcisło, A. A. Finenko, K. Nelson, P. F. Bernath, M. Birk, V. Boudon, A. Campargue, K. V. Chance, A. Coustenis, B. J. Drouin, J.-M. Flaud, R. R. Gamache, J. T. Hodges, D. Jacquemart, E. J. Mlawer, A. V. Nikitin, V. I. Perevalov, M. Rotger, J. Tennyson, G. C. Toon, H. Tran, V. G. Tyuterev, E. M. Adkins, A. Baker, A. Barbe, E. Canè, A. G. Cs'asz'ar, A. Dudaryonok, O. Egorov, A. J. Fleisher, H. Fleurbaey, A. Foltynowicz, T. Furtenbacher, J. J. Harrison, J.-M. Hartmann, V.-M. Horneman, X. Huang, T. Karman, J. Karns, S. Kassi, I. Kleiner, V. Kofman, F. Kwabia-Tchana, N. N. Lavrentieva, T. J. Lee, D. A. Long, A. A. Lukashevskaya, O. M. Lyulin, V. Yu. Makhnev, W. Matt, S. T. Massie, M. Melosso, S. N. Mikhailenko, D. Mondelain, H. S. P. Müller, O. V. Naumenko, A. Perrin, O. L. Polyansky, E. Raddaoui, P. L. Raston, Z. D. Reed, M. Rey, C. Richard, R. T'obi'as, I. Sadiek, D. W. Schwenke, E. Starikova, K. Sung, F. Tamassia, S. A. Tashkun, J. Vander Auwera, I. A. Vasilenko, A. A. Vigasin, G. L. Villanueva, B. Vispoel, G. Wagner, A. Yachmenev, and S. N. Yurchenko. The HITRAN2020 molecular spectroscopic database. *Journal of Quantitative Spectroscopy and Radiative Transfer*, 277:107949, 2022.

[22] G. Li, I.E. Gordon, L.S. Rothman, Y. Tan, S.-M. Hu, S. Kassi, A. Campargue, and E.S. Medvedev. Rovibrational Line Lists for Nine Isotopologues of the CO Molecule in the $X^1/Sigma^+$ Ground Electronic State. *The Astrophysical Journal Supplement Series*, 216:15, 2015.

[23] Y. Tan, F. M. Skinner, S. Samuels, R. J. Hargreaves, R. Hashemi, and I. E. Gordon. H_2, He, and CO_2 line-broadening coefficients, and temperature-dependence exponents for the HITRAN database. Part II: CO_2, N_2O, CO, SO_2 OH, OCS, H_2CO, HCN, PH_3, H_2S and GeH_4, 2021.

[24] C.R. Pollock, F.R. Petersen, D.A. Jennings, and J.S. Wells. Absolute Frequency Measurements of the 2-0 Band of CO at 2.3 μm; Calibration Standard Frequencies from High Resolution Color Center Laser Spectroscopy. *Journal of Molecular Spectroscopy*, 99:357–368, 1983.

[25] Eugene Hecht. *Optics, 5th edition*. Pearson, Harlow, 2017.

[26] T. Gökcen. $N_2 - CH_4 - Ar$ Chemical Kinetic Model for Simulations of Atmospheric Entry to Titan . *AIAA*, 21:9–18, 2004.

[27] C. Park, R. L. Jaffe, and H. Partridge. Chemical-Kinetic Parameters of Hyperbolic Earth Entry. *Journal of Thermophysics and Heat Transfer*, 15:76–90, 2001.

[28] C. Park, J. T. Howe, R. L. Jaffe, and G. V. Candler. Review of Chemical-Kinetic Problems of Future NASA Missions, II: Mars Entries. *Journal of Thermophysics and Heat Transfer*, 8:9–23, 1994.